Soft Matter

PAPER

View Article Online
View Journal | View Issue

Cite this: *Soft Matter*, 2015, **11**, 7296

Nanoparticle stability in biologically relevant media: influence of polymer architecture†

Bethsy Adriana Aguilar-Castillo,[ab] Jose Luis Santos,[a] Hanying Luo,[a] Yanet E. Aguirre-Chagala,[ac] Teresa Palacios-Hernández[ad] and Margarita Herrera-Alonso*[a]

Received 11th June 2015,
Accepted 10th August 2015

DOI: 10.1039/c5sm01455g

www.rsc.org/softmatter

We have contrasted the behavior of nanoparticles formed by the self-assembly of polymers based on poly(ethylene glycol) (PEG) and poly(D,L-lactide), with linear, linear-dendritic and bottle-brush architectures in biologically relevant media. Polymer PEG content ranged between 14% and 46% w/w, and self-assembly was triggered by a rapid and large change in solvent quality inside a four-stream vortex mixer. We examined nanoparticle interaction with human serum albumin (HSA), and solute release in the presence of fetal bovine serum. Dynamic light scattering data showed that PEG surface brushes of all nanoparticles provided effective steric stabilization, thus limiting their interaction with human serum albumin. Calorimetric experiments revealed that nanoparticle–HSA interaction was relatively weak and enthalpically driven, whereas dynamic light scattering results of incubated nanoparticles showed the absence of larger aggregates for most of the polymers examined. Solute core partitioning was examined by the loss of Forster resonance energy transfer (FRET) from a core-loaded donor–acceptor pair. The rate and magnitude of FRET efficiency loss was strongly dependent on the polymer architecture, and was found to be lowest for the bottle-brush, attributed to its covalent nature. Collectively, these findings are expected to impact the molecular design of increasingly stable polymeric carriers for drug delivery applications.

Introduction

The self-assembly of polymer amphiphiles in water, into spherical nanoparticles consisting of a hydrophobic core stabilized by a hydrophilic corona, has been a widely used strategy for the encapsulation and delivery of drugs with low water-solubility or dose-limiting toxicity.[1,2] Enhancing the pharmacologic properties of encapsulated drugs, which generally entails extending systemic circulation, favoring accumulation at target sites, and improving selectivity through active targeting, is dependent on the interaction between nanoparticles and serum proteins. Protein adsorption is the initial step in a cascade of events that ultimately results in elimination *via* opsonization and phagocytosis by macrophages of the reticuloendothelial system.[3,4] The preferred strategy to prevent protein adsorption onto amphiphilic polymer nanoparticles is the use of poly(ethylene glycol) (PEG), a biocompatible and bioresorbable polymer, as the hydrophilic component.

PEG molecular weight is the main determinant of nanoparticle–protein interactions, as it dictates PEG surface density and layer thickness, and in turn, PEG surface conformation (mushroom, brush, and dense brush).[5–8] It is generally agreed that high molecular weight PEG (>2000 Da) will endow nanoparticles with stealth properties,[9] and that higher PEG surface density will reduce protein binding and macrophage uptake, hence prolonging circulation half-lives.[5,10,11]

A great deal of attention has been focused on the study of nanoparticle–protein interactions, particularly for nanoparticles produced by the self-assembly of linear diblock copolymers. However, less so is known regarding the interactions of proteins with nanoparticles from polymers with more complex molecular architectures, which are gaining popularity as a consequence of their unique physicochemical properties; a recent example is Banquy's work on nanoparticles from graft copolymers.[1,12,13] Yet other examples of complex macromolecular architectures are linear-dendritic polymers or dendron-coils, which self-assemble into micelles at concentrations 1–2 orders of magnitude lower

[a] *Department of Materials Science and Engineering, Johns Hopkins University, Baltimore, MD 21218, USA. E-mail: herrera@jhu.edu*
[b] *Instituto de Investigaciones en Materiales, Universidad Nacional Autónoma de México, A.P. 70-360, Coyoacán, Distrito Federal 04510, Mexico*
[c] *Departamento de Ingeniería Química, Facultad de Química, Universidad Nacional Autónoma de México, Distrito Federal 04510, Mexico*
[d] *Departamento de Ciencias Biológicas, Universidad Popular Autónoma del Estado de Puebla, Puebla 72410, Mexico*

† Electronic supplementary information (ESI) available: Experimental section including materials, characterization, methods and experimental procedures, as well as additional figures including NMR spectra, DLS data, FRET kinetic profiles. See DOI: 10.1039/c5sm01455g

than their linear counterparts ($\sim 10^{-8}$ M), and are reported to have high surface coverage of the hydrophilic component.[14,15] These features result in enhanced stabilization at higher dilution, as is the case of injection into the bloodstream, and longer circulation time. Improving nanoparticle stability can also be achieved through the use of unimolecular micelles, among which dendrimers and hyperbranched polymers are the most common examples.[16,17] Other interesting architectures leading to unimolecular micelles, provided they exhibit an optimum hydrophilic/hydrophobic ratio, are multi-arm star amphiphilic block copolymers and molecular brushes (bottle-brushes).[18,19] The covalent nature of these constructs enhances *in vivo* stability and, unlike micellar stabilization by core- or shell-crosslinking, biodegradability and drug release kinetics remain unaffected.[16]

Aside from chemical nature and architectural parameters, the physicochemical properties of polymer assemblies can also be tailored through kinetic manipulation of the assembly process, yielding structures in different states of equilibrium.[20–24] The slow exchange dynamics observed for highly amphiphilic macromolecular systems, along with controlled variations of block chemistry and/or block sizes has led to the discovery of a multitude of aggregates exhibiting unique properties.[20,24,25] Hence, kinetic assembly pathways are also determining factors of the functional properties of polymer based constructs.[23,26,27]

In this study, we have examined the behavior of nanoparticles formed by polymers with different architectures in the presence of biologically relevant media. The polymers studied were based on PEG and poly(D,L-lactide) (PLA), with linear, linear-dendritic (wherein the hydrophilic component is in a dendritic presentation), and bottle-brush architectures. Nanoparticles were formed by a rapid and large change in solvent quality inside a four-stream vortex mixer, and their protein fouling properties were examined in terms of their interaction with human serum albumin, and solute release in the presence of fetal bovine serum.

Experimental

Materials

All reagents were commercially available and used as received unless otherwise specified. 1,8-Diazabicyclo[5.4.0]undec-7-ene (DBU) was kept over activated molecular sieves (3 Å). Racemic 3,6-dimethyl-1,4-dioxane-2,5-dione (D,L-lactide) was purified by recrystallization from anhydrous ethyl acetate twice and dried under high vacuum at room temperature for 24 h prior to use. **1** and **2** were synthesized according to previously reported protocols.[28] Deionized water was purified in a Barnstead Nanopure system to a final resistance of 18.2 mΩ.

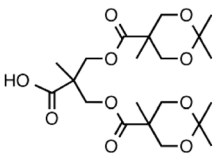

1

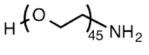

2

Characterization

Details regarding the equipment used for characterization are provided as ESI.†

Methods

Nanoparticle formation. Polymer nanoparticles were produced by a rapid change in solvent quality in a four-stream vortex mixer. A detailed description and characterization of the mixer are provided elsewhere.[29] Polymers were allowed to dissolve in tetrahydrofuran for a minimum of 12 h at room temperature. Solutions were then filtered through 0.22 μm PVDF syringe filters (Millipore). Nanopure water was charged into three 50 mL syringes (Hamilton, NJ) and the organic solution into a 10 mL syringe and mounted on two separate syringe drivers (PHD Ultra, Harvard Apparatus). The THF : water volumetric ratio used was 1 : 9, with mixing speeds of 12 mL min^{-1} and 108 mL min^{-1} (36 mL min^{-1} per stream) for the organic and aqueous phases, respectively. Samples were collected after ~3 s to ensure steady operation of the mixer. Concentrations used for the assembly from linear, linear-dendritic and bottle-brush polymers in THF were 10, 15, and 20 mg mL^{-1}, respectively, resulting in final concentrations of 1, 1.5 and 2.0 mg mL^{-1} in water. Nanoparticle suspensions were then dialyzed (1–8 kDa MWCO, Spectrapor) against Nanopure water for 24 h. Water was replenished every 4 h throughout the dialysis process. Suspensions were stored in clean scintillation vials for further use.

Nanoparticle stability studies. Nanoparticles were incubated at 20 °C in a solution of human serum albumin (2 mg mL^{-1}) in phosphate buffer saline (PBS) 10 mM (pH = 7.4). Nanoparticle concentration in the incubation medium was 0.2 mg mL^{-1}. Samples (in PBS) were placed in a glass cuvette and held at 20 °C during the analysis. Particle size was monitored every hour for the first 8 h of incubation, and subsequently at 12 and 24 h. Standard deviations were estimated based on three separate measurements.

Differential refraction index measurement. Measurements were performed on an Optilab-rEX refractive index detector (Wyatt Technology) at a wavelength of 658 nm. Flow cell temperature was set at 25 °C. Sample and solvent solutions were pumped with a syringe pump (New Era Pump System, NE-1000) at 0.2 mL min^{-1} through a 0.45 μm PVDF syringe filter (Thermo Scientific) prior to measurements. Aggregate solutions were prepared in Nanopure water at the following concentrations: 0.05, 0.06, 0.075, 0.090, 0.1, 0.125, 0.150, 0.175 and 0.200 mg mL^{-1}. (dn/dc) values were analyzed using Astra 6.1 software.

Static light scattering measurements. Static light scattering (SLS) was performed on a Dawn Heleos II (Wyatt Technology) with a 120 mW GaAs linearly polarized laser operating at 658 nm. Sample and solvent solutions were pumped with a syringe pump (New Era Pump System, NE-1000) at 0.2 mL min^{-1} through a 0.45 μm PVDF syringe filter (Thermo Scientific) prior to measurements. Aggregate concentrations measured were 0.05, 0.06, 0.075, 0.09, 0.1, 0.125, 0.15, 0.175 and 0.2 mg mL^{-1}. Dextran sulfate (10 kDa, R_g = 3 nm) was used as an isotropic scatterer to normalize corrected detector voltage 90° to the

detector. The weight-average molecular mass was determined from the angular dependence of the excess absolute light scattered intensity (Rayleigh ratio) as

$$\frac{Kc}{R_\theta} = \frac{1}{M_w}\left(1 + \frac{16\pi^2 n^2 R_g{}^2 \sin^2\left(\frac{\theta}{2}\right)}{3\lambda^2}\right) + 2A_2 c \qquad (1)$$

where $K = (4\pi^2 n^2 (dn/dc)^2/N_A\lambda^4)$ is an optical constant, c is the concentration of the polymer solution in mg mL^{-1}, R_θ is the Rayleigh ratio, θ is the measurement angle, n is the refractive index of the solvent, N_A is Avogadro's constant, (dn/dc) is the refractive index increment, and λ is the wavelength of the laser light in vacuum. The inverse of the molecular weight was obtained from the intercept resultant from the simultaneous extrapolation to zero angles and concentrations. The aggregation number was determined by the ratio of the micelle Mw and the copolymer molecular weight, estimated by ^{1}H NMR.

PEG exposure in nanoparticles by NMR studies. Nanoparticles were concentrated by centrifugation at 5000*g* for 25 min at 19 °C (Allegra 64R, Beckman Coulter) through an Amicon Ultra centrifugal filter (100 kDa MWCO). The concentrated nanoparticle suspension was then transferred to an Eppendorf tube, and to it were added 600 μL D_2O and 3 μL methanol (external reference). Samples were vortexed for 1 min, transferred to NMR tubes and analyzed (Bruker AV 400 MHz). From these solutions, 300 μL were then transferred back to clean scintillation vials, mixed with acetone (1 mL), and sonicated for 10 min. The samples were allowed to dissolve over 4 h and sonicated again for 10 min prior to analysis. Chemical shifts of polymers as unimers (in d_6-acetone) and in nanoparticle form (in D_2O) at room temperature are given in Table S1 (ESI†).

Isothermal titration calorimetry (ITC). ITC measurements were carried out using a VP-ITC titration calorimeter (Microcal/GE Healthcare, Northampton, MA). HSA and nanoparticles were dialyzed against PBS, pH 7.4, and degassed prior to the experiments. The calorimetric cell (~1.4 mL) containing the stirred nanoparticle solution was titrated with 10 μL injections of HSA at a concentration of 10 μM every 300 s, to allow for equilibration. The heat of dilution of HSA was measured in separate experiments where HSA was injected into buffer alone (Fig. S1, ESI†). Saturation was reached in 28 injections. All measurements were carried out at 25 °C. The heat evolved upon each injection of HSA was obtained from the integral of the calorimetric signal. The heat associated with binding of HSA to the nanoparticles was obtained by subtracting the heat of dilution from the heat of reaction. Individual heats were plotted against the molar ratio, and the enthalpy change (ΔH) and association constant ($K_a = 1/K_d$) were obtained by nonlinear regression of the data. Gibbs energy (ΔG) and entropy (ΔS) of interaction were obtained from the relations: $\Delta G = -RT\ln K_a$ and $\Delta S = (\Delta H - \Delta G)/T$, where R is the gas constant and T the absolute temperature.

Forster resonance energy transfer (FRET) experiments. The FRET pair used as acceptor and donor were DiI and DiO (1,1′-dioctadecyl-3,3,3′,3′-tetramethylindocarbocyanine perchlorate and 3,3′-dioctadecyloxacarbocyanine perchlorate), respectively. Dyes were loaded into nanoparticle cores during the rapid assembly process by hydrophobic association. The procedure followed was identical to that described above, except that the organic solution contained the polymer and 1 wt% of each dye. Dye-loaded NP samples were dialyzed for 24 h at room temperature in the dark before FRET measurements. Sample concentration was adjusted to 0.1 mg mL^{-1} and incubated in PBS 10 mM at 37 °C with either FBS100% or FBS10% under gentle agitation. After incubation with FBS, and prior to measurements, nanoparticle suspensions were dialyzed against PBS 10 mM. Time-resolved spectra were measured over 48 h with an excitation wavelength of 484 nm (donor excitation). A control experiment was done, in which equal amounts of DiI and DiO were dissolved directly in 90% fetal bovine serum (FBS) in PBS 10 mM, without nanoparticles (Fig. S2, ESI†). FRET ratio was calculated to monitor the relative peak shift between the emission of DiO (at 501 nm) and the emission of Dil (at 565 nm). The volume ratio of NP solution to FBS 100% was 1 : 9. The volume ratio of NP solution to FBS 10% was 1 : 1.

Polymer synthesis

i. Synthesis of linear diblock copolymers: L45, L75 and L188. Linear diblock copolymers, PLA_{175}-*b*-PEG_{45} (L45), PLA_{175}-*b*-PEG_{75} (L75), and PLA_{175}-*b*-PEG_{188} (L188), wherein the subscripts represent repeat units of each block, were synthesized by ring-opening polymerization of D,L-lactide from poly(ethylene glycol)methylether (mPEG) macroinitiators. A detailed protocol for this synthesis, and the resulting ^{1}H NMR spectra, are provided as ESI† (Fig. S3–S5).

ii. Synthesis of linear-dendritic copolymer D45, ***5****.* The linear-dendritic copolymer, possessing a hydrophilic dendritic segment, was synthesized by a three-step reaction, consisting of: (a) synthesis of a hydroxyl terminated dendron, (b) polymerization of D,L-lactide from the hydroxyl terminated dendron, and (c) poly(ethylene glycol) conjugation to the distal ends of the PLA-dendron. Detailed protocols for each step of the reaction, and the corresponding NMR spectra, are also provided as ESI† (Fig. S6–S8).

iii. Synthesis of the bottle brush polymer B45, ***6****.* The protocol for the synthesis of B45 was adapted from Chen, and previously reported.[30] Its ^{1}H NMR spectrum is provided as Fig. S9 (ESI†).

Results and discussion

The structures and characteristics of the different polymers examined are provided in Fig. 1 and Table 1.

As noted in the Experimental section, self-assembly was triggered by a rapid change in solvent quality inside a four-stream vortex mixer, to a final solvent : non-solvent ratio of 1 : 9 (v/v).[29,31] Nanoparticle morphology was examined by transmission electron microscopy, and spherical aggregates were observed in all cases (Fig. 2), with number average diameters ranging from 19 to 39 nm. Dynamic light scattering analysis revealed *z*-average particle sizes ranged from 28 to 44 nm, with monomodal particle distributions and relatively narrow polydispersities in water (Table 2). The differences between these

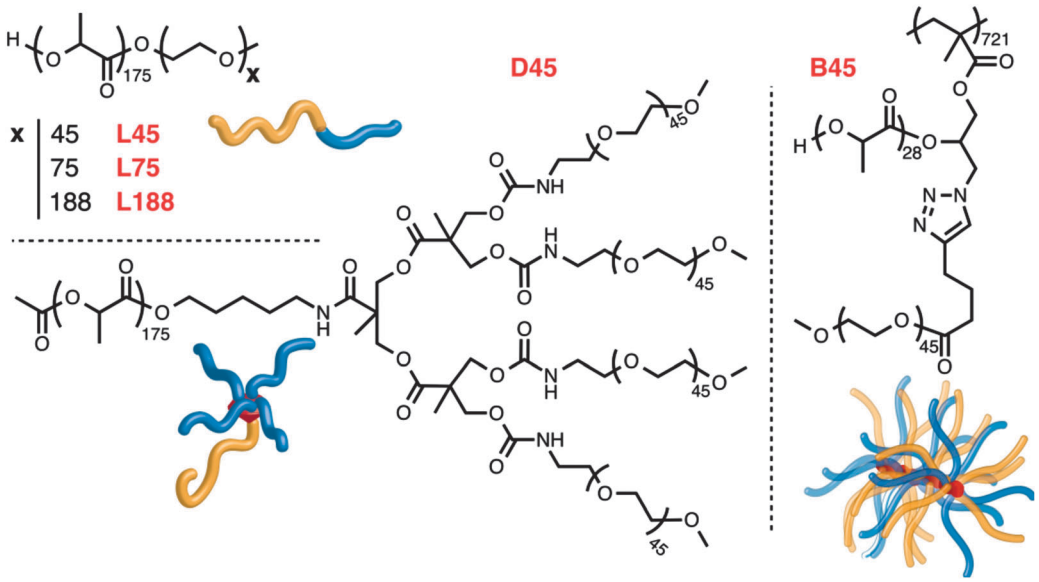

Fig. 1 Structures and schematics of the polymers examined. Numbers in the identifiers of linear (L45, L75 and L188), linear-dendritic (D45), and brush-like (B45) copolymers represent the number of PEG repeat units. PEG blocks are shown in blue, PLA in yellow, the dendron core in orange, and the PGMA backbone in red. The schematic of the brush polymer is meant to represent only a segment of the chain.

Table 1 Polymers used in this study

	Polymer architecture	w_{PEG} [a] (wt%)	M_n [a] (kDa)	M_n [b] (kDa)	M_w [b] (kDa)	$Đ_M$ [b]
L45	Linear	14.4	13.9	14.0	15.0	1.07
L75	Linear	21.5	15.3	15.0	16.9	1.06
L188	Linear	40.9	20.3	22.1	22.9	1.03
D45	Linear-dendritic	39.2	20.4	14.2	16.3	1.14
B45	Brush	45.7	3.15×10^6	—	—	—

[a] Estimated from ^{1}H NMR. [b] Measured by gel permeation chromatography.

two measurements are attributed to the type of average used (number *vs.* *z*-), as well as undersizing due to dehydration in TEM, the extent of which will be influenced by the hydrophilic fraction of the polymer (w_{PEG}).

Aggregation numbers (N_w^{agg}) were determined by comparing the apparent nanoparticle molecular weight determined by SLS ($M_{w,app}$) to that of the unimer ($M_{w,unimer}$), which was considered to be equivalent to the number average molecular weight obtained from NMR.[32] For a given hydrophobic block size, an increase in hydrophilic block length of linear copolymers resulted in a decrease of the aggregation number, as previously shown.[33] A decrease in particle size, which generally accompanies a change in the aggregation number,[32,34,35] was only observed on increasing hydrophilic block length from 45 to

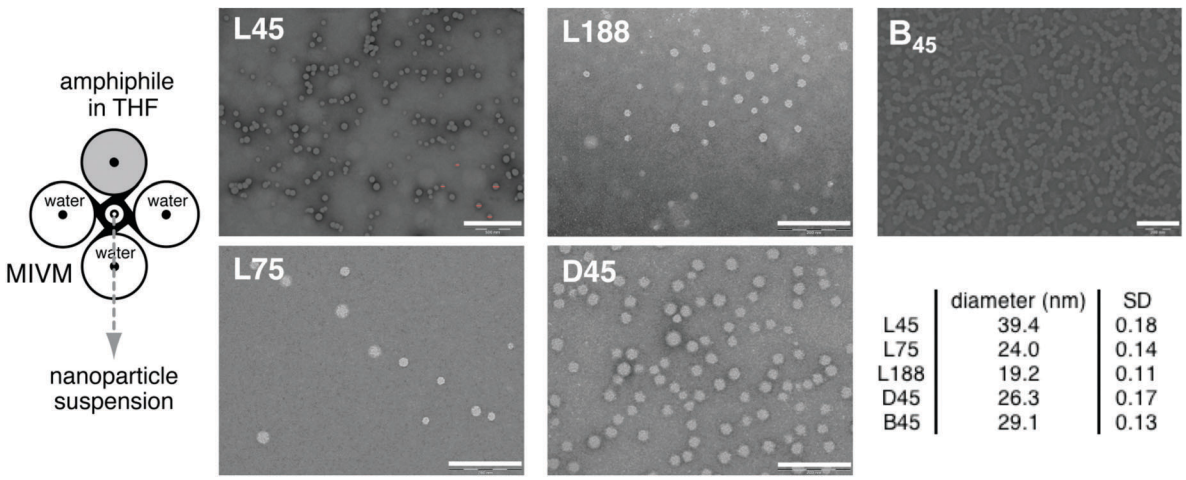

Fig. 2 Polymer self-assembly was triggered by rapid change in solvent quality (from THF, to THF : H_2O = 1 : 9 v : v) inside a multi-inlet vortex mixer (schematic on the left). Particle morphology was examined by TEM after dialysis against water to remove the organic solvent. Spherical aggregates were observed in all cases. Scale bars correspond to 200 nm for all but L45 (500 nm scale bar). A summary table of TEM diameters (number average) and their standard deviation is also provided.

Table 2 Characterization of nanoparticle suspensions

	D_h[a] (nm)	PDI[a]	$M_{w,app}$[b] (Da, 10^5)	N_w^{agg}[c]	PEG exposure[d] (%)	ζ[e] (mV) H_2O	ζ[e] (mV) PBS (10 mM)
L45	39.5	0.17	22.9	165	78.6	−31.2	−4.2
L75	29.7	0.18	11.0	71	90.9	−28.8	−2.5
L188	29.3	0.17	7.2	35	93.1	−13.3	−1.7
D45	27.9	0.19	12.1	59	—	−26.0	−4.4
B45	43.7	0.15	31.5	1	92.7	−22.8	−3.9

[a] Nanoparticle hydrodynamic radii and polydispersity indices (PDI) were determined by dynamic light scattering. [b] Apparent molecular weight was measured by static light scattering. [c] Nanoparticle aggregation numbers were estimated according to $N_w^{agg} = M_{w,app}/M_{w,unimer}$, where $M_{w,unimer}$ was taken to be equivalent to the number average molecular weight obtained from NMR. [d] PEG surface exposure was measured by ^{1}H NMR. [e] Zeta potentials were measured by electrophoretic light scattering.

75 repeat units; no significant changes were observed thereafter. Aggregation numbers of nanoparticles from diblock copolymers ranged from 35 to 165. Interestingly, although the hydrophilic content (w_{PEG}) of D45 is very similar to that of L188, its aggregation number is closer to that of L75. We attribute this to the architecture of the dendritic hydrophilic block, in which the dendron serves as a focal point for PEG presentation. If, rather than using hydrophilic content as the basis for comparison, we use the radius of gyration of the hydrophilic block, which is very similar between L75 and D45 (8.4 *vs.* 8.3 nm, respectively),[36] it is reasonable these nanoparticles have similar aggregation numbers. Finally, SLS data revealed that B45 collapsed into a unimolecular particle, which we attribute to its hydrophilic content and long backbone.[37]

The low aggregation numbers observed can be explained in terms of the nanoparticle assembly method, which relies on a large and rapid change in solvent quality, resulting in kinetically-arrested structures. The mechanism leading to the formation of kinetically frozen nanoparticles is best described by a diffusion-limited fusion process, wherein small aggregates form by the association of hydrophobically collapsed blocks, diffuse toward each another, and fuse to form structures with larger aggregation numbers.[31] This process continues until the hydrophilic block reaches a critical concentration on the surface, corresponding to the brush regime. Evolution to more thermodynamically stable structures, by micelle fusion or fission or unimer exchange, is generally unfavorable given the low quality of the solvent. In this early stage of association, the aggregation number is predicted to be a fraction of that achieved at equilibrium ($N_{agg,eq}^{5/9}$),[38] which would explain the low values measured for all but the bottle-brush polymer.

The rapid nucleation process leading to nanoparticle formation, along with the similarity of solubility parameters between PLA and PEG (δ = 21.4 MPa$^{1/2}$ and δ = 21.3 MPa$^{1/2}$ for PEG_{5k} and PLA_{10k}, respectively),[39] may lead to embedding of PEG chains inside the nanoparticle core. To examine this, we carried out NMR studies of nanoparticles suspended in D_2O. Whereas in a good solvent (d_6-acetone), complete structural resolution of L45, L75, L188 and B45 is observed, only the PEG signal is evident when the particles are suspended in D_2O, suggesting that PLA forms a central hydrophobic solid-like core (Fig. S11–S14, ESI†). This was expected, since well resolved PLA signals from PEG-*b*-PLA nanoparticles have only been observed for systems with considerably shorter PLA blocks (<4 kDa) or at higher temperatures (50 °C and 70 °C), and explained in terms of increased polymer mobility.[40] The use of an external standard (methanol) allowed for quantification of PEG on nanoparticle surfaces relative to the total PEG content. As shown in Table 2, PEG exposure increases with w_{PEG}, exceeding 90% for all but L45, which exhibits ~79% exposure. This trend is in agreement with linear diblock copolymer systems.[32] Interestingly, PEG exposure from the bottle-brush polymer is also high (93%), suggesting its efficient arrangement into a core–shell type structure, despite the lower conformational degrees of freedom attributed to the PGMA backbone. In contrast, nanoparticles from PEG/PLA graft copolymers with a PLA backbone and PEG_{45} side-chains, exhibited lower surface exposure (~75%) for w_{PEG} between 15–40%.[13] Overall, these results are consistent with nanoparticles exhibiting a solid-like PLA core, stabilized by a solubilized PEG corona.[39–41]

Nanoparticle surface charge was measured by electrophoretic light scattering; zeta-potentials are provided in Table 2, in water and phosphate buffer saline (PBS). In water, all nanoparticles exhibit a negative surface charge, explained by incomplete screening of the core-forming PLA block by surface PEG chains.[42] Bare PLA nanoparticles are reported to have surface charge ranging from −50 mV to −70 mV.[43,44] In the case of NPs from linear copolymers, surface charge decreased with increasing hydrophilic content from −31 to −13 mV, suggesting that L188 screens the underlying PLA core more effectively than the shorter chains of L45. Surface charges of D45 and B45 are in the intermediate range. In a buffered medium, a noticeable drop in zeta potential was observed for all nanoparticles, with surface charge ranging only from −2 mV to −4 mV. Despite the small differences in ζ potentials among samples, their near neutrality confirms effective screening of surface charges by the PEG blocks regardless of polymer architecture or w_{PEG}.

PEG surface conformation is a critical parameter influencing nanoparticle stability. It can be deduced by comparing the Flory radius (R_F) of surface chains,[5,7] to either the distance between PEG grafting points (D), or the thickness of the PEG layer (L). These are defined as,

$$R_F = \alpha N^{3/5} \quad (2)$$

where α is the persistence length (0.35 nm for PEG), and N is the number of repeat units. Nanoparticle core radius (R_c) was calculated according to,[45,46]

$$R_c = \left[\frac{3N_{agg}M_{w,PLA}}{4\pi N_A \rho_{PLA}}\right]^{1/3} \quad (3)$$

where N_{agg} is the aggregation number measured by SLS, N_A is Avogadro's number, and $M_{w,PLA}$ and ρ_{PLA} are the molecular weight and density of the PLA block, respectively. The contribution of the PGMA backbone of B45 is not considered in this calculation as it represents only a small fraction (~4 wt%) of the total mass. PEG surface density (σ, chains per nm^2) was calculated as,[5,47]

$$\sigma = \frac{N_w^{agg}}{4\pi R_c^2} \quad (4)$$

Table 3 PEG surface conformation

	w_{PEG}[a] (wt%)	R_F[b] (nm)	R_c[c] (nm)	σ[d] (chains per nm^2)	D[e] (nm)	L[f] (nm)	PEG conformation
L45	14.4	3.4	8.6	0.18	2.7	5.5	Brush
L75	24.2	4.7	6.5	0.14	3.1	6.3	Brush
L188	40.9	8.1	5.1	0.11	3.4	9.5	Brush
D45	39.2	3.4	6.1	0.51	1.6	5.9	Brush
B45	45.7	3.4	7.7	0.96	1.1	7.3	Dense brush

[a] Determined from ^{1}H NMR. [b] Flory radius. [c] Nanoparticle core radius. [d] PEG surface density. [e] Distance between PEG grafts. [f] PEG layer thickness.

where N_w^{agg} is the aggregation number measured by SLS. Finally, the distance between PEG grafts (D) and PEG layer thickness (L) are given by,[7,48]

$$D = \frac{4R_c}{\sqrt{N_w^{agg}}} \quad (5)$$

$$L = \alpha N^{3/5}\left(\frac{R_c}{D}\right)^{2/5} \quad (6)$$

Results for all polymers are presented in Table 3. It is relevant to mention that measured PEG surface exposure was not taken into account for these calculations as it is considered to be high for most nanoparticles. PEG surface coverage can be categorized into three conformational regimes: "mushroom", "brush", and "dense brush". In the first, $D > R_F$ and low chain extension results in the formation of a thin PEG layer. In the "brush" regime, $D \sim R_F$ and chains extend farther away from the nanoparticle surface, resulting in increased PEG layer thickness. Finally, at very high surface coverage, $L > 2R_F$ and the chains form a "dense brush". It is generally agreed that higher PEG surface density will reduce protein binding and macrophage uptake, hence prolonging circulation half-lives.[5,10,11] Based on these equations, PEG chains from the polymers examined adopt a brush conformation on nanoparticle surfaces, in agreement with the rapid assembly mechanism.[31] The unimolecular micelle has a higher PEG brush density, which falls within the dense brush regime. In all cases, PEG density exceeds 0.1 chains per nm^2, the lower limit for serum protein adsorption on planar surfaces.[49] For linear copolymers, both D and L increase with hydrophilic content, while a notable decrease in the distance between graft points is observed when comparing L75 to D45 which have similar aggregation numbers, and attributed to the dendritic hydrophilic block of the latter, from which four PEG chains are presented per dendron base.

Colloidal stability

We examined colloidal stability in the context of protein adsorption experiments. In this sense, nanoparticle stability was evaluated in 10 mM PBS for 24 h in the absence of proteins. Average particle size and size distributions at room temperature and at 37 °C are shown in Fig. S15 and S16 (ESI†), along with the corresponding values in the absence of buffer at room temperature (shaded regions).

Size variations of PEGylated nanoparticles upon incubation in high ionic strength media are common, and largely attributed to a reduction of electrostatic repulsion between particles.[42] This was also observed to be the case for PEG/PLA nanoparticles made from grafted copolymers, as shown by Banquy *et al.*[13] At higher temperatures, increased disruption of the hydrogen bonding between PEG and water would further contribute to agglomeration.[50] In our case, there was an initial size increase all particles on incubation, the extent of which was dependent on the type of polymer and temperature. Nanoparticles from B45 were the most stable in buffer at the two temperatures examined. Size variation for nanoparticles from L45, L75, D45 and particularly L188, were more substantial, especially at higher temperature. Nevertheless, these variations are small in comparison to data reported in the literature.[43] We attribute this effect to a combination of core swelling by solvent partitioning and intraparticle rearrangement at constant aggregation number,[31] both of which could also be associated with the assembly process used. The rapid change in solvent quality triggering association, results in particles with low aggregation numbers which could possibly favor more solvent partitioning. Water in the core may act as a plasticizer for the PLA block,[40] enabling more intraparticle rearrangement at higher temperature. Nevertheless, the results indicate that steric, and not electrostatic, effects provided by the external PEG layer, effectively stabilize nanoparticles and prevent their agglomeration.

Nanoparticle interaction with biologically relevant media

Having established nanoparticle behavior in PBS, we examined nanoparticle interaction with human serum albumin (HSA), and solute stabilization in the presence of fetal bovine serum (FBS). Interaction with HSA was evaluated by isothermal titration calorimetry (ITC) and dynamic light scattering; solute release in the presence of FBS was assessed by fluorescence spectroscopy.

Nanoparticle–HSA interaction

ITC is adirect and reliable technique for quantifying nanoparticle–protein interactions which has been used to elucidate the behavior of a number of different nanoparticle–protein combinations.[5,51–53] Briefly, nanoparticle suspensions of known concentrations (Table 4), were titrated with HSA to saturation.

Table 4 Thermodynamic parameters of nanoparticle–HSA interaction, per mol of HSA

	[NP][a] (μM)	ΔG (kJ mol^{-1})	ΔH (kJ mol^{-1})	$T\Delta S$ (kJ mol^{-1} K^{-1})	K_a[b] (1×10^6, M^{-1})	N[c]
L45	0.41	−37.3 ± 0.2	−97.7 ± 4.9	−59.6 ± 6.0	3.43 ± 0.28	1.70 ± 0.02
L75	0.91	−37.5 ± 0.2	−132.1 ± 10.8	−95.4 ± 11.8	3.73 ± 0.35	0.69 ± 0.01
L188	1.31	−37.3 ± 0.3	−243.9 ± 46.1	−205.7 ± 44.7	3.47 ±0.45	0.23 ± 0.02
D45	1.16	−37.5 ± 0.2	−102.9 ± 6.1	−65.6 ± 5.9	3.73 ± 0.34	0.51 ± 0.01
B45	0.57	−37.4 ± 0.2	−172.9 ± 12.5	−134.2 ± 11.9	3.93 ± 0.30	0.89 ± 0.03

[a] Nanoparticle concentrations used in ITC experiments. [b] Association constant. [c] Binding stoichiometry.

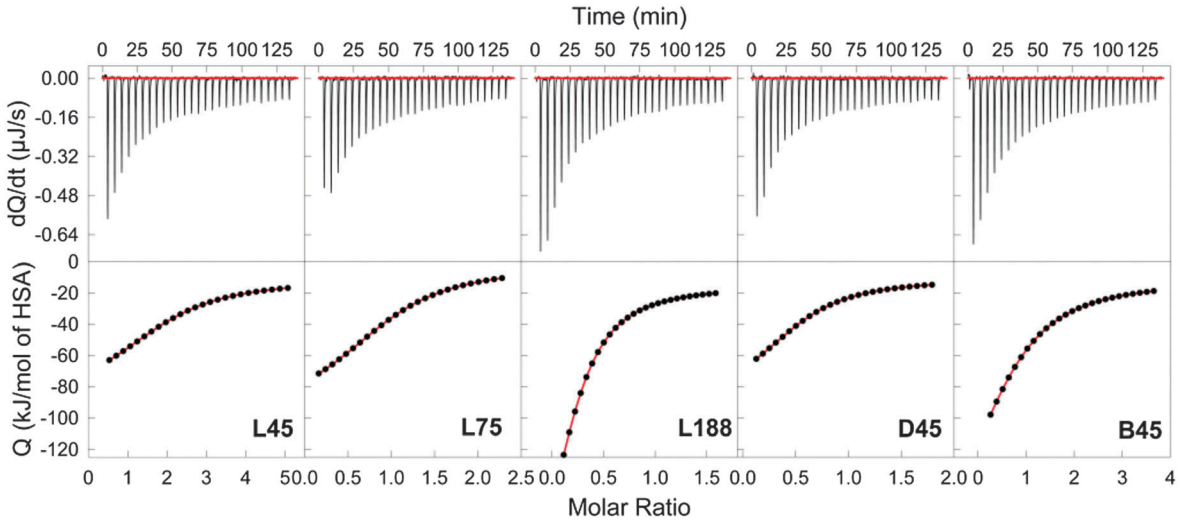

Fig. 3 Titration profiles of HSA titrated into NP solutions in PBS. Nanoparticle concentrations are provided in Table 4. Upper panels correspond to raw data; the bottom row shows experimental data (solid circles), and the fit to a one-site binding model according to the non-linear Levenberg–Marquardt fitting algorithm (red line) after subtraction of heat of dilution of the protein.

The heat evolved in each injection was obtained from the integral of the calorimetric signal (Fig. 3, top row). Heats associated with NP–HSA binding were calculated by subtracting the heat of dilution of HSA in buffer (Fig. S1, ESI†), from the heat of reaction. Individual heats were plotted against the molar ratio (protein : nanoparticle), from which the enthalpy change (ΔH), association constant (K_a), and stoichiometry (n) were derived by nonlinear regression using the Levenberg–Marquardt fitting algorithm according to a single-site binding model (Fig. 3, bottom row). The extracted thermodynamic parameters of NP–HSA interaction correspond to an average of duplicate experiments.

Human serum albumin (HSA) is the most abundant protein in plasma, known for its extraordinary ligand-binding capacity, its capability as a biomarker, and used clinically to treat a number of diseases.[54] In the context of nanoparticle–serum interaction, it is typically the first protein to undergo adsorption, and can therefore greatly influence *in vivo* nanoparticle biodistribution.[55,56]

As revealed from the shape of the titration curves, HSA was observed to bind to all nanoparticles, exhibiting an exothermic association in all cases. Data were satisfactorily fit to a single-site binding model, from which the thermodynamic parameters were extracted and are summarized in Table 4. The observed favorable NP–protein association ($\Delta G < 0$) results from favorable enthalpy changes ($\Delta H < 0$), partially offset by unfavorable entropic loss ($\Delta S < 0$).[5,7,52] As all nanoparticles are nearly electrostatically neutral under the conditions used for ITC, the enthalpic driving force is attributed to a combination of weak non-covalent forces such hydrogen bonding and/or van der Waals interactions, rather than electrostatic effects.

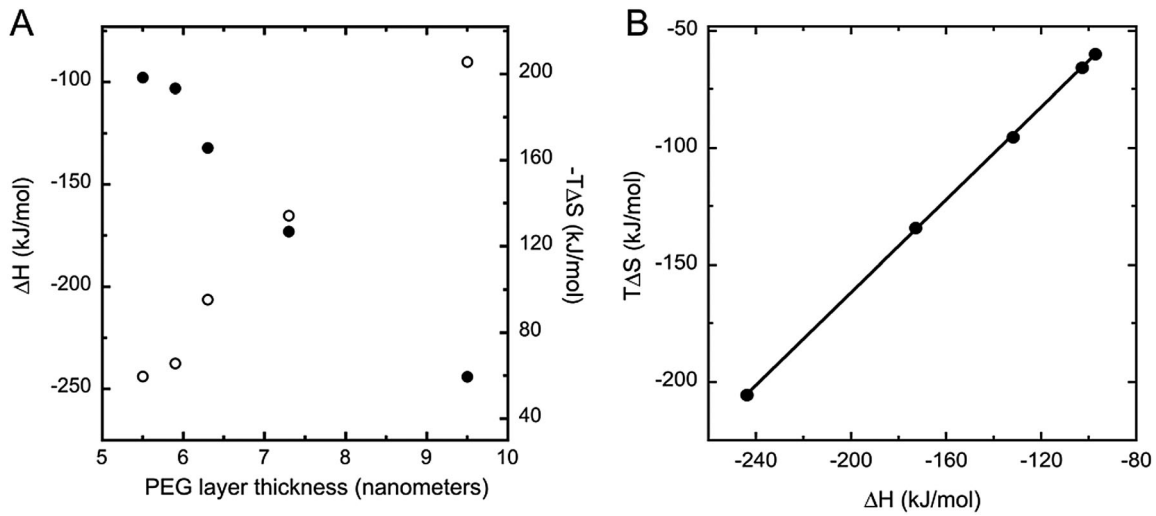

Fig. 4 Effect of PEG layer thickness on binding enthalpy (filled circles) and entropy (empty circles) (A), and enthalpy–entropy compensation effect for NP–HSA interaction (B). The intercept and slope of the latter curve were $T\Delta S_0 = 0.99$ and $\alpha = 36.9$ kJ mol^{-1}.

Small variations were observed among the association constants of all polymers, pointing to relatively weak ($K_a \sim 10^6\ M^{-1}$) NP–HSA binding. This was recently suggested, albeit not quantified, for the interaction between bovine serum albumin (BSA, a protein similar to HSA) and PEG/PLA nanoparticles from graft copolymers.[13] Binding stoichiometry ranged from ~0.2–2, indicating only a small number of binding events per nanoparticle. There is, however, a clear effect of increasing entropic and enthalpic contributions with PEG layer thickness, which may be influenced by the underlying polylactide core surface (Fig. 4A). Nevertheless, there is a near invariance of ΔG among all samples, as shown by the trends of the data in Fig. 4A. This effect has been explained in terms of enthalpy–entropy compensation: increasing enthalpy change is accompanied by greater entropic loss due to NP–protein complex ordering, resulting in small changes in free energy. In the context of nanoparticles, enthalpy–entropy compensation has been observed for their interaction with proteins,[57] as well as polysaccharides.[58] Graphically, compensation can be observed in the linear dependence between ΔH and $T\Delta S$. The relationship between the two is given by,[57]

$$T\Delta S = T\Delta S_0 + \alpha\Delta H \quad (7)$$

where the intercept ($T\Delta S_0$) and slope (α) provide quantitative measures of desolvation and conformational changes that takes place upon complex formation, respectively.

While in the aforementioned examples, the range of ΔH and $T\Delta S$ is considerably broader than in our case, we also observed a linear relationship between these parameters, as shown in Fig. 4B. A linear regression of the data yielded a slope of 0.99 and an intercept of 36.9 kJ mol^{-1}. The slope was the same as that found by Shea *et al.* (0.99),[58] and smaller than that estimated by Rotello *et al.* (1.07),[57] indicating that conformational change of protein–NP binding observed in our system compares better with that existing between cross-linked hydrogels and polysaccharides, than that between proteins and gold nanoparticles monolayers. The intercept, on the other hand, appeared to be larger for PEG-containing nanoparticles (36.9 kJ mol^{-1}), than AuNPs (35.2 kJ mol^{-1}) or cross-linked hydrogel nanoparticles (34.9 kJ mol^{-1}), indicating that desolvation is more entropically favored for the former.

Dynamic light scatting studies were also used to examine the interaction between nanoparticles and HSA. DLS is a useful characterization technique as shifts in nanoparticle peak position are indicative of adsorption.[59–61] Under the conditions examined, the molar excess of protein with respect to nanoparticle ranged

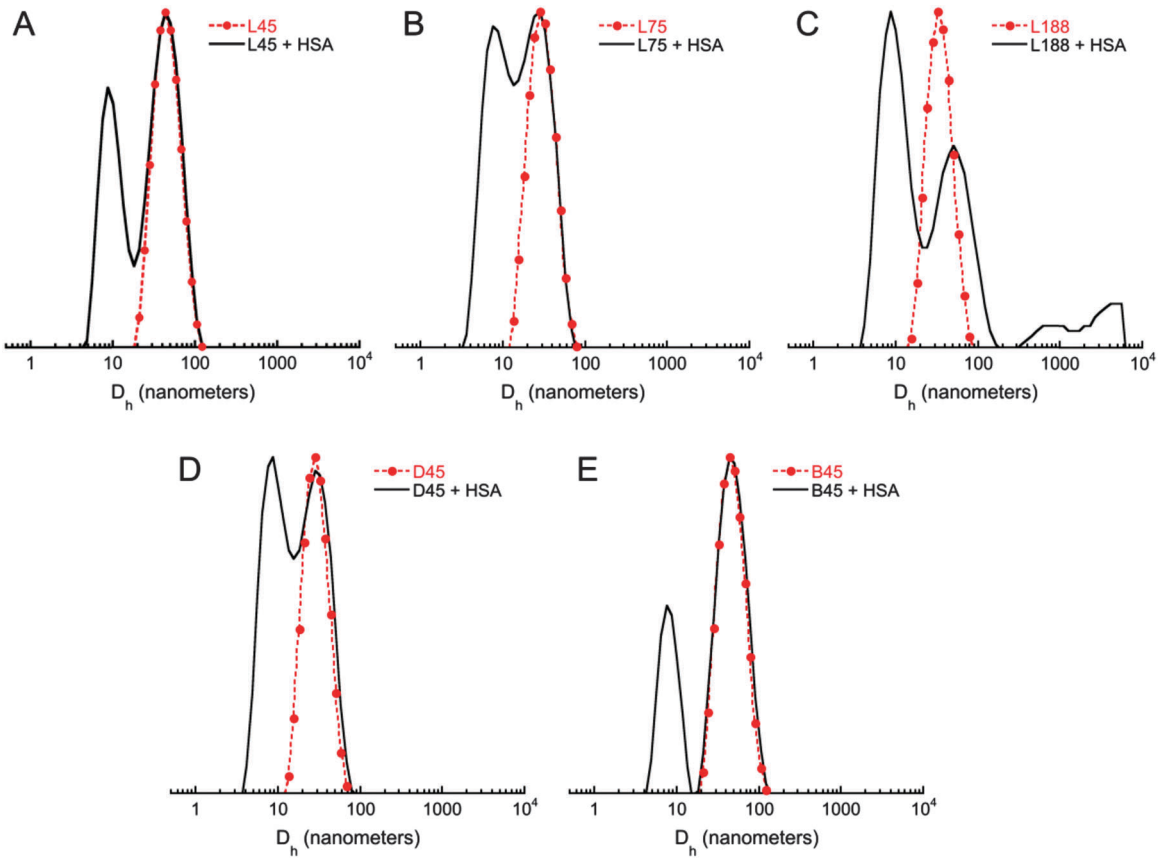

Fig. 5 Size distributions of nanoparticles in the presence of human serum albumin (HSA) after 24 h incubation in PBS 10 mM and 20 °C. HSA and polymer concentrations were kept at 2 mg mL^{-1} and 0.2 mg mL^{-1}. As aggregation numbers vary according to each polymer, 0.2 mg mL^{-1} corresponds to: L45 (8.7×10^{-5} mM), L75 (1.8×10^{-4} mM), L188 (2.8×10^{-4} mM), D45 (1.6×10^{-4} mM), and B45 (6.3×10^{-5} mM). Distributions of nanoparticles in phosphate buffer saline are also shown for reference (dotted lines).

from 11- to 47-fold. DLS traces of mixtures, along with the peak corresponding to the nanoparticles in PBS, are provided in Fig. 5. The protein peak is centered at D_h = 8.7 nm.

NP–HSA size distributions were bimodal in all cases. For all samples except L188, there was only a small shift in nanoparticle peak position after incubation with the protein, indicating the absence of larger aggregates. Furthermore, the ratio of intensities of nanoparticle and protein (I_{NP}/I_{HSA}) varied according to the polymer as: B45 (1.78) > L45 (1.28) > L75 (1.04) > D45 (0.95). We explain the difference of NP peak intensity to the combined effects of particle size and protein binding. Nanoparticles from B45 and L45 are the largest of all (see Table 2), so despite their lower concentration relative to other nanoparticles, their scattering intensity may be high based on size considerations. Furthermore, L45 and B45 also exhibited higher binding stoichiometry, which would explain the lower intensity of the peak attributed to the protein. The opposite applies to L75 and D45, which are not only smaller but also have lower binding stoichiometry. On the other hand, L188 which had the lowest stoichiometry of all, shows not only a considerable shift of the nanoparticle peak to higher values, but also other signals at larger sizes, which suggest the formation of large protein-mediated aggregates.

Release of lipophilic compounds from nanoparticles

The stability of lipophilic compounds in nanoparticle cores was determined by incubation with fetal bovine serum (FBS), and monitored by measuring the Forster resonance energy transfer (FRET) of the lipophilic donor–acceptor pair.[2,62,63] FRET occurs when nanoparticles loaded with a donor–acceptor pair are excited at the excitation wavelength of the donor and emit at the emission wavelength of the acceptor, provided the distance between the FRET pair allows for efficient energy transfer between the two chromophores. As solutes are released over time, the distance between chromophores is no longer within the permissible range for FRET. As a result, a shift of the emission wavelength occurs from that of the acceptor, to that of the donor. The decrease of FRET efficiency has been linked to nanoparticle disassembly, and shown to depend strongly on FBS concentration.[2]

The FRET pair consisting of DiO (donor, λ_{exc} = 488 nm, λ_{emi} = 501 nm) and DiI (acceptor, λ_{emi} = 565 nm) was used for these experiments. Loaded nanoparticles (containing 1 wt% of each dye)

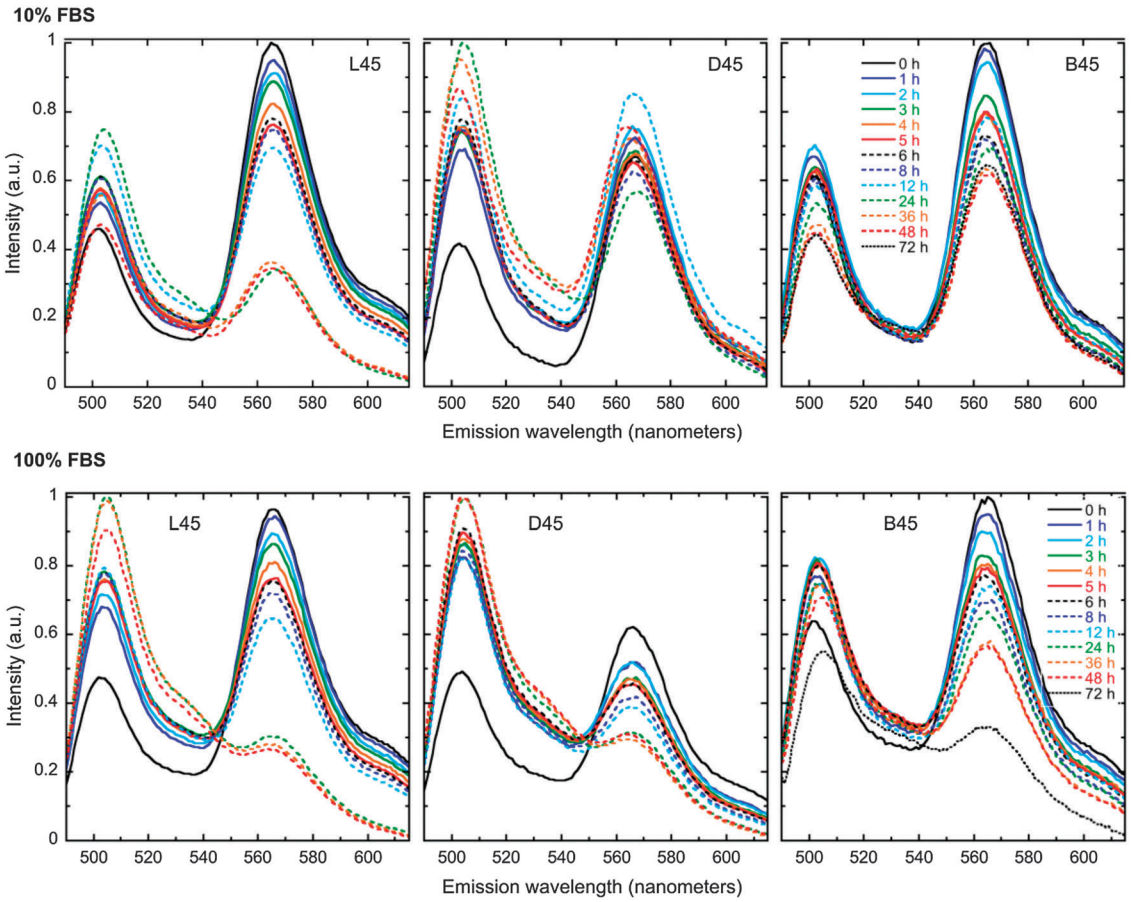

Fig. 6 FRET measurements during nanoparticle incubation in fetal bovine serum, showing the shift in primary emission peak from that of the acceptor (DiI, I_{565}) to that of the donor (DiO, I_{501}). Shown are FRET experiments for L45, D45 and B45; remaining spectra are given in Fig. S17 (ESI†). Nanoparticles were incubated in 10 mM PBS, 37 °C in 10% FBS (top row) and 100% FBS (bottom row). Fluorescence measurements for linear and linear-dendritic copolymers (L45, L75, L188, D45) were carried out over 48 h, and over 72 h for the brush polymer (B45).

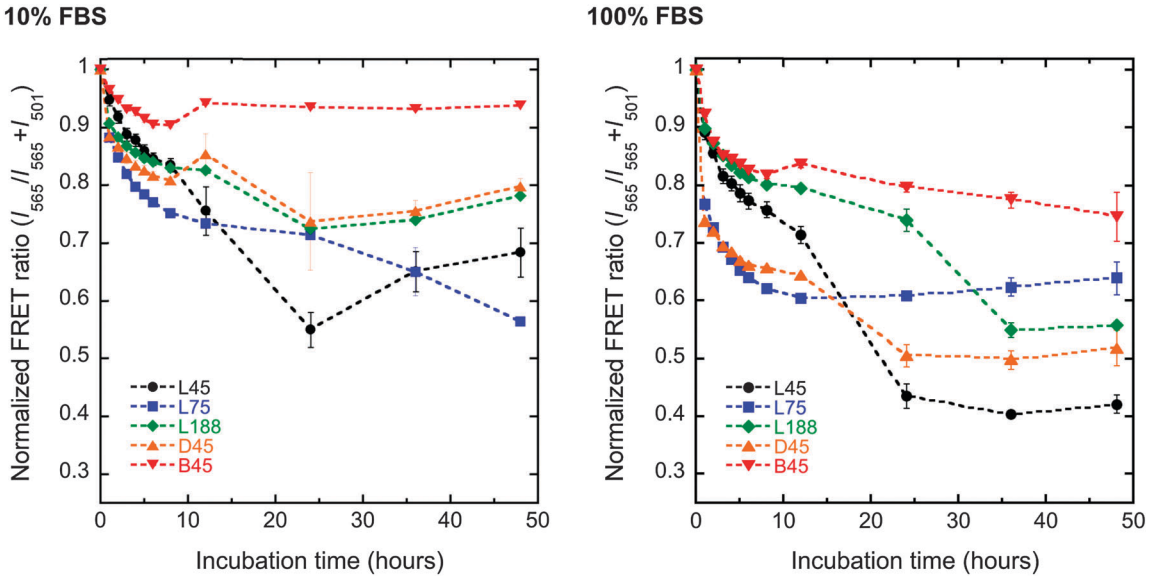

Fig. 7 Normalized FRET ratios (FR) during incubation in 10% and 100% fetal bovine serum (FBS). The extent of nanoparticle dissociation at 48 h (right) was estimated by comparing the fluorescence intensity of a nanoparticle-free solution (corresponding to 100% dissociation), to that of nanoparticle suspensions.

were formed following the rapid assembly method used before. The apparent FRET ratio (FR, or FRET efficiency) was estimated from emission intensities (I) of each chromophore as: FR = $I_{565}/I_{565} + I_{501}$.

Time-resolved spectra of select nanoparticles in 10% and 100% FBS, are shown in Fig. 6; loaded nanoparticles in PBS 10 mM were used as controls (Fig. S18, ESI†). Fluorescence from B45 nanoparticles, was measured to 72 h; data acquisition was stopped after 48 h for the remaining samples. FRET ratios were calculated and are shown in Fig. 7. Again, loaded nanoparticles in PBS 10 mM were used as controls (Fig. S19, ESI†). As a control experiment, FRET efficiency was measured for a sample containing 90% FBS and the donor–acceptor pair (DiI/DiO) at the same concentrations used for encapsulation studies (Fig. S2, ESI†). For this sample FR = 0.48, which would suggest co-localization of the FRET pair in a hydrophobic reservoir present in the complex protein mixture of FBS. This value, which corresponds to the minimum attainable FR in serum, is similar to that obtained by Lu and Shoichet,[2] and is independent of chromophore concentration.

As shown in Fig. 6 and 7, all nanoparticles showed a decrease in FRET efficiency in the presence of FBS, the magnitude of which was sensitive to the type of polymer and serum concentration. In the absence of serum, only a small ($<10\%$) variation in FRET efficiency was observed (Fig. S18, ESI†), demonstrating nanoparticle stability. In general, more solute release was observed for samples incubated at higher FBS concentration, the only exception being L75, for reasons yet unknown to us.

In the presence of FBS, all nanoparticles showed a shift of the primary emission peak,[63,64] the rate and magnitude of which was sensitive to the type of polymer and serum concentration. Relating FRET efficiency to nanoparticle stability would suggest that the most stable were unimolecular bottle-brush nanoparticles, with a 5% loss in efficiency in 10% FBS, and a 20% loss in 100% FBS. In contrast, the most unstable nanoparticles in the presence of serum are those formed by L45, which show a drop in FRET efficiency of 30% in 10% serum, and 60% in 100% FBS. The behavior of the remaining samples falls between these extremes. It is interesting to note that, despite having hydrophilic components with the same molecular weight, nanoparticles from B45 are considerably more stable than those of L45, which we attribute to a stabilizing effect associated with the presence of the backbone.

Conclusions

In summary, the interaction between HSA or FBS with PEG/PLA nanoparticles formed by polymers with different architectures, was examined using a combination of DLS, SLS, ITC and FRET. The results showed that despite the rapid method used for their formation, nanoparticles from PEG/PLA polymers with either linear, linear-dendritic or brush-like structures exhibited high PEG exposure, resulting in good steric stability in buffered media and at elevated temperature, particularly in the case of the brush polymer. Steric stabilization provided by PEG brushes limited nanoparticle interaction with HSA, which was relatively weak ($K_a \sim 10^6\ M^{-1}$) and enthalpically driven. Favorable enthalpic and unfavorable entropic contributions were found to increase with PEG layer thickness. Finally, solute core partitioning was highly dependent on the architecture of the polymer, and was found to be the lowest for the brush polymer, attributed to its covalent nature. These findings are expected to impact the molecular design of increasingly stable amphiphilic polymer carriers for drug delivery applications.

Acknowledgements

We thank Professor Rafael Herrera-Nájera (Facultad de Química, Universidad Nacional Autónoma de México) for valuable discussions, Professor Ernesto Freire and Dr Arne Schön (Department of Biology, JHU) for the use of the ITC. Y.E.A.-C. and B.A.A.-C. were supported by CONACyT through its visiting student program "*Programa de becas mixtas en el extranjero*". Scholarship number for B.A.A.-C. is 204358. T.P.-H. is also supported through CONACyT through its postdoctoral program *"Estancias Posdoctorales al Extranjero para la Consolidación de Grupos de Investigation"* (Award number 236893). Financial support was provided by The Johns Hopkins University as start-up funds and an NSF CAREER Award to M.H.-A. (DMR 1151535).

References

1 J. Logie, S. C. Owen, C. K. McLaughlin and M. S. Shoichet, *Chem. Mater.*, 2014, **26**, 2847–2855.
2 J. Lu, S. C. Owen and M. S. Shoichet, *Macromolecules*, 2011, **44**, 6002–6008.
3 C. D. Walkey and W. C. W. Chan, *Chem. Soc. Rev.*, 2012, **41**, 2780–2799.
4 A. A. Shemetov, I. Nabiev and A. Sukhanova, *ACS Nano*, 2012, **6**, 4585–4602.
5 J. L. Perry, K. G. Reuter, M. P. Kai, K. P. Herlihy, S. W. Jones, J. C. Luft, M. Napier, J. E. Bear and J. M. DeSimone, *Nano Lett.*, 2012, **12**, 5304–5310.
6 Q. Yang, S. W. Jones, C. L. Parker, W. C. Zamboni, J. E. Bear and S. K. Lai, *Mol. Pharmaceutics*, 2014, **11**, 1250–1258.
7 S. Louguet, A. C. Kumar, N. Guidolin, G. Sigaud, E. Duguet, S. Lecommandoux and C. Schatz, *Langmuir*, 2011, **27**, 12891–12901.
8 C. D. Walkey, J. B. Olsen, H. B. Guo, A. Emili and W. C. W. Chan, *J. Am. Chem. Soc.*, 2012, **134**, 2139–2147.
9 A. Hucknall, S. Rangarajan and A. Chilkoti, *Adv. Mater.*, 2009, **21**, 2441–2446.
10 F. Alexis, E. Pridgen, L. K. Molnar and O. C. Farokhzad, *Mol. Pharmaceutics*, 2008, **5**, 505–515.
11 K. Knop, R. Hoogenboom, D. Fischer and U. S. Schubert, *Angew. Chem., Int. Ed.*, 2010, **49**, 6288–6308.
12 C. Garofalo, G. Capuano, R. Sottile, R. Tallerico, R. Adami, E. Reverchon, E. Carbone, L. Izzo and D. Pappalardo, *Biomacromolecules*, 2014, **15**, 403–415.
13 J. M. Rabanel, J. Faivre, S. F. Tehrani, A. Lalloz, P. Hildgen and X. Banquy, *ACS Appl. Mater. Interfaces*, 2015, **7**, 10374–10385.
14 J. W. Bae, R. M. Pearson, N. Patra, S. Sunoqrot, L. Vukovic, P. Kral and S. Hong, *Chem. Commun.*, 2011, **47**, 10302–10304.
15 H. J. Hsu, S. Sen, R. M. Pearson, S. Uddin, P. Kral and S. Hong, *Macromolecules*, 2014, **47**, 6911–6918.
16 Y. L. Xiao, H. Hong, A. Javadi, J. W. Engle, W. J. Xu, Y. A. Yang, Y. Zhang, T. E. Barnhart, W. B. Cai and S. Q. Gong, *Biomaterials*, 2012, **33**, 3071–3082.
17 J. T. Guo, H. Hong, G. J. Chen, S. X. Shi, Q. F. Zheng, Y. Zhang, C. P. Theuer, T. E. Barnhart, W. B. Cai and S. Q. Gong, *Biomaterials*, 2013, **34**, 8323–8332.
18 O. G. Schramm, G. M. Pavlov, H. P. van Erp, M. A. R. Meier, R. Hoogenboom and U. S. Schubert, *Macromolecules*, 2009, **42**, 1808–1816.
19 J. Guo, H. Hong, G. Chen, S. Shi, T. R. Nayak, C. P. Theuer, T. E. Barnhart, W. Cai and S. Gong, *ACS Appl. Mater. Interfaces*, 2014, **6**, 21769–21779.
20 H. G. Cui, Z. Y. Chen, S. Zhong, K. L. Wooley and D. J. Pochan, *Science*, 2007, **317**, 647–650.
21 C. Charbonneau, C. Chassenieux, O. Colombani and T. Nicolai, *Macromolecules*, 2011, **44**, 4487–4495.
22 T. Nicolai, O. Colombani and C. Chassenieux, *Soft Matter*, 2010, **6**, 3111–3118.
23 R. C. Hayward and D. J. Pochan, *Macromolecules*, 2010, **43**, 3577–3584.
24 J. H. Zhu, S. Y. Zhang, K. Zhang, X. J. Wang, J. W. Mays, K. L. Wooley and D. J. Pochan, *Nat. Commun.*, 2013, **4**, 2297.
25 S. Jain and F. S. Bates, *Macromolecules*, 2004, **37**, 1511–1523.
26 C.-W. Wang, D. Sinton and M. G. Moffitt, *J. Am. Chem. Soc.*, 2011, **133**, 18853–18864.
27 J. T. Zhu and R. C. Hayward, *J. Am. Chem. Soc.*, 2008, **130**, 7496–7502.
28 J. L. Santos and M. Herrera-Alonso, *Macromolecules*, 2013, **47**, 137–145.
29 Y. Liu, C. Y. Cheng, Y. Liu, R. K. Prud'homme and R. O. Fox, *Chem. Eng. Sci.*, 2008, **63**, 2829–2842.
30 H. Luo, J. L. Santos and M. Herrera-Alonso, *Chem. Commun.*, 2014, **50**, 536–538.
31 B. K. Johnson and R. K. Prud'homme, *Phys. Rev. Lett.*, 2003, **91**, 118302.
32 T. Riley, S. Stolnik, C. R. Heald, C. D. Xiong, M. C. Garnett, L. Illum, S. S. Davis, S. C. Purkiss, R. J. Barlow and P. R. Gellert, *Langmuir*, 2001, **17**, 3168–3174.
33 I. LaRue, M. Adam, E. B. Zhulina, M. Rubinstein, M. Pitsikalis, N. Hadjichristidis, D. A. Ivanov, R. I. Gearba, D. V. Anokhin and S. S. Sheiko, *Macromolecules*, 2008, **41**, 6555–6563.
34 J. P. Hinestrosa, J. Alonzo, M. Osa and S. M. Kilbey, *Macromolecules*, 2010, **43**, 7294–7304.
35 T. P. Lodge, J. A. Bang, Z. B. Li, M. A. Hillmyer and Y. Talmon, *Faraday Discuss.*, 2005, **128**, 1–12.
36 J. L. Santos and M. Herrera-Alonso, *Macromolecules*, 2014, **47**, 137–145.
37 H. Y. Luo, J. L. Santos and M. Herrera-Alonso, *Chem. Commun.*, 2014, **50**, 536–538.
38 E. E. Dormidontova, *Macromolecules*, 1999, **32**, 7630–7644.
39 K. M. Pustulka, A. R. Wohl, H. S. Lee, A. R. Michel, J. Han, T. R. Hoye, A. V. McCormick, J. Panyam and C. W. Macosko, *Mol. Pharmaceutics*, 2013, **10**, 4367–4377.
40 C. R. Heald, S. Stolnik, K. S. Kujawinski, C. De Matteis, M. C. Garnett, L. Illum, S. S. Davis, S. C. Purkiss, R. J. Barlow and P. R. Gellert, *Langmuir*, 2002, **18**, 3669–3675.
41 A. Vila, H. Gill, O. McCallion and M. J. Alonso, *J. Controlled Release*, 2004, **98**, 231–244.
42 J. V. Jokerst, T. Lobovkina, R. N. Zare and S. S. Gambhir, *Nanomedicine*, 2011, **6**, 715–728.
43 Y. C. Dong and S. S. Feng, *Biomaterials*, 2004, **25**, 2843–2849.

44 J. Thevenot, A.-L. Troutier, L. David, T. Delair and C. Ladavière, *Biomacromolecules*, 2007, **8**, 3651–3660.
45 B. H. Tan, H. Hussain, Y. Liu, C. B. He and T. P. Davis, *Langmuir*, 2009, **26**, 2361–2368.
46 X. Li, K. Y. Mya, X. Ni, C. He, K. W. Leong and J. Li, *J. Phys. Chem. B*, 2006, **110**, 5920–5926.
47 D. Bazile, C. Prudhomme, M. T. Bassoullet, M. Marlard, G. Spenlehauer and M. Veillard, *J. Pharm. Sci.*, 1995, **84**, 493–498.
48 T. M. Birshtein, O. V. Borisov, Y. B. Zhulina, A. R. Khokhlov and T. A. Yurasova, *Polym. Sci.*, 1987, **29**, 1293–1300.
49 M. Malmsten, K. Emoto and J. M. Van Alstine, *J. Colloid Interface Sci.*, 1998, **202**, 507–517.
50 T. Riley, T. Govender, S. Stolnik, C. D. Xiong, M. C. Garnett, L. Illum and S. S. Davis, *Colloids Surf., B*, 1999, **16**, 147–159.
51 S. Lindman, I. Lynch, E. Thulin, H. Nilsson, K. A. Dawson and S. Linse, *Nano Lett.*, 2007, **7**, 914–920.
52 A. Asadi, A. A. Saboury, A. A. Moosavi-Movahedi, A. Divsalar and M. N. Sarbolouki, *Int. J. Biol. Macromol.*, 2008, **43**, 262–270.
53 T. Cedervall, I. Lynch, S. Lindman, T. Berggård, E. Thulin, H. Nilsson, K. A. Dawson and S. Linse, *Proc. Natl. Acad. Sci. U. S. A.*, 2007, **104**, 2050–2055.
54 G. Fanali, A. di Masi, V. Trezza, M. Marino, M. Fasano and P. Ascenzi, *Mol. Aspects Med.*, 2012, **33**, 209–290.
55 L. Vroman and A. L. Adams, *ACS Symp. Ser.*, 1987, **343**, 154–164.
56 P. Aggarwal, J. B. Hall, C. B. McLeland, M. A. Dobrovolskaia and S. E. McNeil, *Adv. Drug Delivery Rev.*, 2009, **61**, 428–437.
57 M. De, C. C. You, S. Srivastava and V. M. Rotello, *J. Am. Chem. Soc.*, 2007, **129**, 10747–10753.
58 Z. Y. Zeng, J. Patel, S. H. Lee, M. McCallum, A. Tyagi, M. D. Yan and K. J. Shea, *J. Am. Chem. Soc.*, 2012, **134**, 2681–2690.
59 H. Pan, M. Qin, W. Meng, Y. Cao and W. Wang, *Langmuir*, 2012, **28**, 12779–12787.
60 L. Calzolai, F. Franchini, D. Gilliland and F. Rossi, *Nano Lett.*, 2010, **10**, 3101–3105.
61 T. A. Larson, P. R. Joshi and K. Sokolov, *ACS Nano*, 2012, **6**, 9182–9190.
62 H. Chen, S. Kim, W. He, H. Wang, P. S. Low, K. Park and J. X. Cheng, *Langmuir*, 2008, **24**, 5213–5217.
63 H. T. Chen, S. W. Kim, L. Li, S. Y. Wang, K. Park and J. X. Cheng, *Proc. Natl. Acad. Sci. U. S. A.*, 2008, **105**, 6596–6601.
64 X. Hu, J. Hu, J. Tian, Z. Ge, G. Zhang, K. Luo and S. Liu, *J. Am. Chem. Soc.*, 2013, **135**, 17617–17629.